

Dynamical polarization of graphene at finite doping

B. Wunsch^{1,2}, T. Stauber², F. Sols¹, and F. Guinea²

¹ Departamento de Física de Materiales, Facultad de Ciencias Físicas,
Universidad Complutense de Madrid, E-28040 Madrid, Spain.

² Instituto de Ciencia de Materiales de Madrid, CSIC, Cantoblanco, E-28049 Madrid, Spain.

(Dated: February 8, 2020)

The polarization of graphene is calculated exactly within the random phase approximation for arbitrary frequency, wave vector, and doping. At finite doping, the static susceptibility saturates to a constant value for low momenta. At $q = 2\mu/\hbar v_F$ it has a discontinuity only in the second derivative. In the presence of a charged impurity this results in Friedel oscillations which decay with same power law as the Thomas Fermi contribution, the latter being always dominant. The spin density oscillations in the presence of a magnetic impurity are also calculated. The dynamical polarization for low q and arbitrary ω is employed to calculate the dispersion relation and the decay rate of plasmons and acoustic phonons as a function of doping. The low screening of graphene, combined with the absence of a gap, leads to a significant stiffening of the longitudinal acoustic lattice vibrations.

PACS numbers: 63.20.-e, 73.20.Mf, 73.21.-b

I. INTRODUCTION

Recent progress in the isolation of single graphene layers has permitted the realization of transport and Raman experiments¹ which have stimulated an intense theoretical research on the properties of a monoatomic graphene sheet. Most of the unusual electronic properties can be understood in terms of a simple tight-binding approach for the π -electrons of carbon, which yields a gapless linear band structure with a vanishing density of states at zero doping.^{2,3}

The electronic band structure of an undoped single graphene sheet allows for a description of the electronic properties in terms of an effective field theory which is equivalent to Quantum Electrodynamics (QED) in 2+1 dimensions. Within such a framework important physical quantities such as the electron self-energy or the charge and spin susceptibilities can be calculated exploiting the special symmetries of the model.⁴

Finite doping away from half-filling qualitatively changes the above description, since it breaks electron-hole symmetry and also the pseudo Lorentz invariance needed for the equivalence with QED in two space dimensions. One is thus forced to retreat to conventional condensed-matter techniques such as e.g. Matsubara Green's functions. This was recently done by Ando⁵, who calculated the static susceptibility of graphene at finite doping. Similar calculations for bulk graphite had been performed by Shung *et al.*,⁶ who investigated the dielectric function and the plasmon behavior. Studies of static screening in graphene based on the Thomas-Fermi approximation had also been considered.^{7,8} The relation between the polarization and the transport properties of graphene has been recently discussed in Refs. 5,9,10.

In this paper, we calculate the dynamical polarization within the random phase approximation (RPA) for arbitrary wavevector, frequency, and doping. We discuss the method of calculation in the next section. We present in

Section III results for static screening, where we analyze the Friedel oscillations induced by a charged or magnetic impurity, comparing our results with those of the two-dimensional electron gas (2DEG). Section IV discusses the plasmon dispersion relation and lifetime. In Section V we analyze the screening of the longitudinal acoustic modes by the conduction electrons. Finally, Section VI presents the main conclusions of our work. Some of the more technical aspects of the formalism are explained in the Appendix.

II. RPA CALCULATION

Within the effective mass approximation, and focusing on one of the two inequivalent K -points, the Hamiltonian of an hexagonal graphene sheet is given in the Bloch spinor representation as²

$$H = \hbar v_F \sum_{\mathbf{k}} H_{\mathbf{k}} \quad , \quad H_{\mathbf{k}} = \psi_{\mathbf{k}}^{\dagger} \begin{pmatrix} \mu/v_F & \phi_{\mathbf{k}} \\ \phi_{\mathbf{k}}^* & \mu/v_F \end{pmatrix} \psi_{\mathbf{k}} . \quad (1)$$

Here $\phi_{\mathbf{k}} = k_x + ik_y$ and $\psi_{\mathbf{k}} = (a_{\mathbf{k}}, b_{\mathbf{k}})^T$, where $a_{\mathbf{k}}$ and $b_{\mathbf{k}}$ are the destruction operators of the Bloch states of the two triangular sublattices. We have also introduced the chemical potential μ which explicitly breaks the space-time equivalence of relativistic QED. The Fermi velocity $v_F = 3at/2\hbar$ is determined by the carbon-carbon distance $a = 1.42$ Å and the nearest neighbor hopping energy $t = 2.7$ eV resulting in $v_F = 8.76 \times 10^5$ m/s.¹¹ We note that the effective Hamiltonian given above is valid only for wave vectors $k < \Lambda$, where $\Lambda \simeq 8.25$ eV is a high-energy cutoff stemming from the discreteness of the lattice.¹¹

The quantity of interest for many physical properties is the dynamical polarization, since it determines e.g. the effective electron-electron interaction, the Friedel oscillations and the plasmon and phonon spectra. In terms

of the bosonic Matsubara frequencies $\omega_n = 2\pi n/\beta$, it is defined as¹²

$$P(\mathbf{q}, i\omega_n) = -\frac{1}{A} \int_0^\beta d\tau e^{i\omega_n \tau} \langle T\rho(\mathbf{q}, \tau)\rho(-\mathbf{q}, 0) \rangle, \quad (2)$$

where A denotes the area. The average is taken over the canonical ensemble and the density operator is given by the sum of the density operators of the two sub-lattices $\rho = \rho_a + \rho_b$. This amounts to working in the long-wavelength limit. To first order in the electron-electron interaction, we obtain

$$P^{(1)}(\mathbf{q}, i\omega_n) = \frac{g_S g_V}{4\pi^2} \int d^2 k \sum_{s, s' = \pm} f^{ss'}(\mathbf{k}, \mathbf{q}) \times \frac{n_F(E^s(k)) - n_F(E^{s'}(|\mathbf{k} + \mathbf{q}|))}{E^s(k) - E^{s'}(|\mathbf{k} + \mathbf{q}|) - i\hbar\omega_n}, \quad (3)$$

with $E^\pm(k) = \pm\hbar v_F k - \mu$ the eigenenergies, $n_F(E) = (e^{\beta E} + 1)^{-1}$ the Fermi function, and $g_S = g_V = 2$ the spin and valley degeneracy. A characteristic difference between the polarization of graphene and that of a 2DEG is the appearance of the prefactors $f^{ss'}(\mathbf{k}, \mathbf{q})$ coming from the band-overlap of the wave functions^{5,6}

$$f^{ss'}(\mathbf{k}, \mathbf{q}) = \frac{1}{2} \left(1 + ss' \frac{k + q \cos \varphi}{|\mathbf{k} + \mathbf{q}|} \right), \quad (4)$$

where φ denotes the angle between \mathbf{k} and \mathbf{q} .

At zero temperature, the Fermi functions yield simple step functions. We define the following retarded function by replacing $i\omega_n \rightarrow \omega + i\delta$

$$\chi_D^\pm(\mathbf{q}, \omega) = \frac{g}{4\pi^2 \hbar} \int_{k \leq D} d^2 k \sum_{\alpha = \pm} \alpha f^\pm(\mathbf{k}, \mathbf{q}) \times \frac{1}{\omega + \alpha v_F(k \mp |\mathbf{k} + \mathbf{q}|) + i\delta}, \quad (5)$$

where $g \equiv g_S g_V$. The $(+)(-)$ sign corresponds to intra(inter)-band transitions and D is a general upper limit.

For $\mu = 0$, the retarded polarization thus reads

$$P_0^{(1)}(\mathbf{q}, \omega) = -\chi_\Lambda^-(\mathbf{q}, \omega). \quad (6)$$

For $\mu > 0$, i.e., for nonzero electron doping, the retarded polarization has an additional term

$$\Delta P^{(1)}(\mathbf{q}, \omega) = \chi_\mu^+(\mathbf{q}, \omega) + \chi_\mu^-(\mathbf{q}, \omega). \quad (7)$$

In the Appendix we give additional details of the calculation of Eq. (5). Here we summarize these expressions in terms of two complex functions, $F(q, \omega)$ and $G(x)$, defined as

$$F(q, \omega) = \frac{g}{16\pi} \frac{\hbar v_F^2 q^2}{\sqrt{\omega^2 - v_F^2 q^2}},$$

$$G(x) = x\sqrt{x^2 - 1} - \ln \left(x + \sqrt{x^2 - 1} \right). \quad (8)$$

From now on it is always assumed that $\omega > 0$, noting that the polarization for $\omega < 0$ is obtained via $P^{(1)}(\mathbf{q}, -\omega) = [P^{(1)}(\mathbf{q}, \omega)]^*$. Equations (6) and (7) are then rewritten in the following compact form

$$P^{(1)}(\mathbf{q}, \omega) = P_0^{(1)}(\mathbf{q}, \omega) + \Delta P^{(1)}(\mathbf{q}, \omega), \quad (9)$$

with

$$P_0^{(1)}(q, \omega) = -i\pi \frac{F(q, \omega)}{\hbar^2 v_F^2}, \quad (10)$$

and

$$\Delta P^{(1)}(q, \omega) = -\frac{g\mu}{2\pi\hbar^2 v_F^2} + \frac{F(q, \omega)}{\hbar^2 v_F^2} \left\{ G\left(\frac{\hbar\omega + 2\mu}{\hbar v_F q}\right) - \Theta\left(\frac{2\mu - \hbar\omega}{\hbar v_F q} - 1\right) \left[G\left(\frac{2\mu - \hbar\omega}{\hbar v_F q}\right) - i\pi\right] - \Theta\left(\frac{\hbar\omega - 2\mu}{\hbar v_F q} + 1\right) G\left(\frac{\hbar\omega - 2\mu}{\hbar v_F q}\right) \right\}. \quad (11)$$

Equations (9)-(11) are the main result of this work. Details of the calculation are given in the Appendix, where we also give expressions for the real and imaginary part of the polarization in terms of real functions.

Two limits of the polarization are of particular importance: (i) The long wavelength limit $q \rightarrow 0$ with $\omega > v_F q$ fixed, which is relevant for optical spectroscopy and for the plasma dispersion. (ii) The static case $\omega = 0$ with q arbitrary, which is relevant for the screening of charged or magnetic impurities.

For the first case we obtain

$$P^{(1)}(q \rightarrow 0, \omega) = \frac{gq^2}{8\pi\hbar\omega} \left[\frac{2\mu}{\hbar\omega} + \frac{1}{2} \ln \left| \frac{2\mu - \hbar\omega}{2\mu + \hbar\omega} \right| - i\frac{\pi}{2} \Theta(\hbar\omega - 2\mu) \right]. \quad (12)$$

And for the second case we recover the result obtained by Ando⁵

$$P^{(1)}(q, 0) = -\frac{g\mu}{2\pi\hbar^2 v_F^2} + \Theta(\hbar v_F q - 2\mu) \frac{gq}{8\pi\hbar v_F} G_< \left(\frac{2\mu}{\hbar v_F q} \right), \quad (13)$$

where $G_<(x) \equiv -iG(x)$ is the real function (for $|x| < 1$) given in Eq. (A2). Note that for $2\mu \leq \hbar v_F q \leq \Lambda$ the absolute value of the polarization is linear in q , and acquires rapidly the behavior of $P_0^{(1)}$. By contrast, the polarization of the ordinary 2DEG decreases with increasing wave vector for $q > 2k_F$. Furthermore, and also in contrast to the 2DEG, where the first derivative of the static polarization is discontinuous at $q = 2k_F$, doped graphene has a continuous first derivative at $\hbar v_F q = 2\mu$ and a discontinuous second derivative.

Table I summarizes the ω dependence of $|\text{Im}P^{(1)}|$ for $q \rightarrow 0$ for a 2DEG and for doped graphene. While the

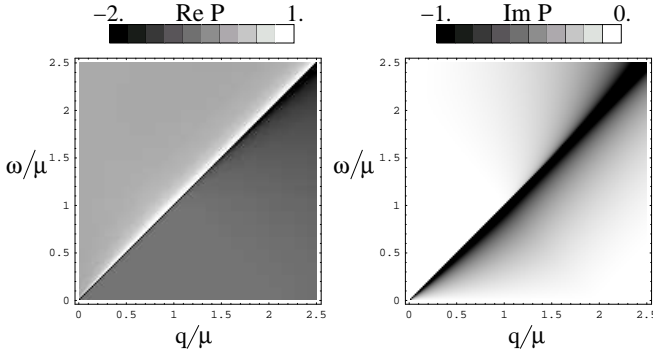


FIG. 1: Density plot of $\text{Re}P^{(1)}(q, \omega)$ (left) and $\text{Im}P^{(1)}(q, \omega)$ (right) in units of μ/v_F^2 . We set $\hbar = v_F = 1$.

	$y < 1$	$y = 1$	$y > 1$
2DEG	ω	$\omega^{1/2}$	0
graphene	ω	$\omega^{3/2}$	0

TABLE I: Low-frequency dependence of $|\text{Im}P^{(1)}|$ in the limit $q \rightarrow 0$ for a 2DEG and for doped graphene. Here $y \equiv \hbar v_F q / 2\mu$.

dependence is the same for $\hbar v_F q \neq 2\mu$, a subtle difference appears at $\hbar v_F q = 2\mu$. This difference is intimately related to the nonanalytic behavior (as a function of q) of the static polarization at $\hbar v_F q = 2\mu$. It leads to e.g. a different power law decay of the electron screening, as will be shown in subsection III. Table I also indicates that, depending on the order in which the limits $q, \mu \rightarrow 0$ are taken, the low-frequency behavior may be that of an insulator, a metal, or a hybrid between the two.

The polarization is a continuous function of q and ω except for the square-root divergence which $P(q, \omega)$ shows at $\omega = v_F q$. Figure 1 shows real and imaginary parts of the polarization given by Eq. (9). We note that $\text{Im}P^{(1)}(q, \omega) = 0$ for $\hbar v_F q < \hbar \omega < 2\mu - \hbar v_F q$ or $0 < \hbar \omega < \hbar v_F q - 2\mu$, and negative otherwise, while $\text{Re}P^{(1)}(q, \omega) < 0$ for $\omega < v_F q$.

The divergence at $\omega = v_F q$ vanishes in the self-consistent RPA result of the polarization given by¹³

$$P_{\text{RPA}}(\mathbf{q}, \omega) = \frac{P^{(1)}(\mathbf{q}, \omega)}{1 - v_q P^{(1)}(\mathbf{q}, \omega)}. \quad (14)$$

Here $v_q = e^2/2\kappa_0 q$ denotes the in-plane Coulomb potential in vacuum. We note that $P_{\text{RPA}}(q, v_F q) = -v_q$ so that the self-consistent polarization has a real and finite value at $\omega = v_F q$. Figure 2 shows real and imaginary parts of the self-consistent polarization. While the singularity at $\omega = v_F q$ is absent, a new singularity appears in $\text{Re}P_{\text{RPA}}(q, \omega)$ at $\omega \propto \sqrt{q}$, which reflects the existence of plasmons, as will be discussed in subsection IV.

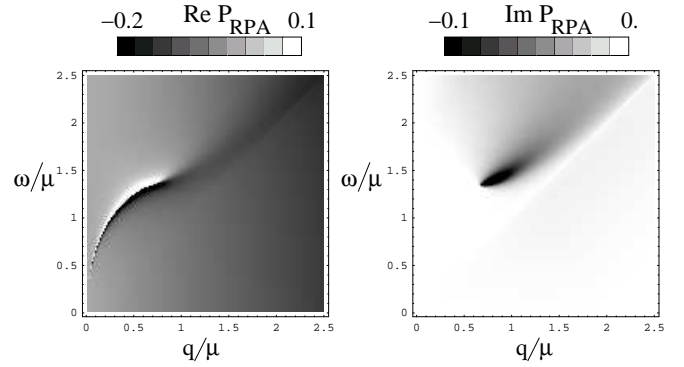


FIG. 2: Same as Fig. 1, for the renormalized polarization $P_{\text{RPA}}(q, \omega)$.

III. STATIC SCREENING

An external charge density $n^{\text{ext}}(\mathbf{r}) = Ze\delta(\mathbf{r})$ is screened by free electrons due to the Coulomb interaction. This results in the induced charge density $\delta n(r)$

$$\delta n(r) = \frac{Ze}{4\pi^2} \int d^2 q \left[\frac{1}{\epsilon(q, 0)} - 1 \right] e^{i\mathbf{q} \cdot \mathbf{r}}. \quad (15)$$

Here $\epsilon(q, 0) \equiv \lim_{\omega \rightarrow 0} \epsilon(q, \omega)$. Within the RPA approximation⁶

$$\epsilon(q, \omega) = \epsilon_0 - v_q P^{(1)}(q, \omega). \quad (16)$$

The effective dielectric constant ϵ_0 includes high energy screening processes. We take $\epsilon_0 \simeq 2.4$.⁵

There are two contributions to the induced charge density. A non-oscillating part comes from the long-wavelength behavior of the polarization. This contribution is obtained within the Thomas-Fermi (TF) approximation and is given by

$$\delta n_{\text{TF}}(r) \simeq -\frac{Ze\hbar v_F}{2\pi\alpha g\mu r^3}, \quad (17)$$

where $\alpha \equiv e^2/4\pi\kappa_0\hbar v_F \simeq 2.5$. We note here that in a 2DEG the TF contribution also decays as r^{-3} .¹⁵

The second contribution to the long distance behavior is oscillatory and comes from the non-analyticity of the polarization at $\hbar v_F q = 2\mu$.^{14,15} However, and quite importantly, in graphene the non-analyticity results from a discontinuity occurring only in second derivative, the first derivative being continuous. This leads to an oscillatory decay

$$\delta n_{\text{osc}}(r) \propto \frac{Ze\hbar v_F \cos(2\mu r)}{\mu(\epsilon_0 + 2\alpha)^2 r^3}, \quad (18)$$

which contrasts with the behavior of a 2DEG, where Friedel oscillations scale like $\delta n(r) \propto \cos(2k_F r) r^{-2}$. This difference has been previously noted in Refs. 8,16, where

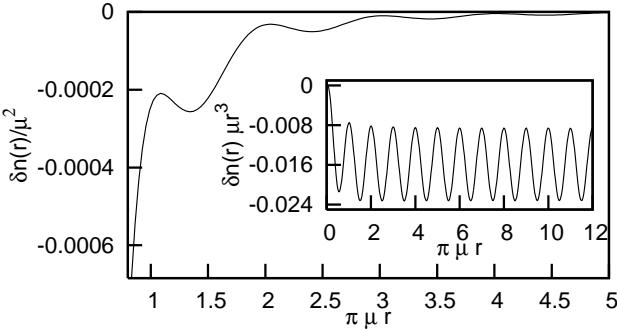


FIG. 3: Induced charge density $\delta n(r)$ (in units of $\mu^2 Ze$) as a function of the dimensionless variable $\pi \mu r$. The inset shows the r^{-3} decay at large distances. The high frequency screening is set to $\epsilon_0 = 2.4$. In the used representation the graphs are invariant under a change of the chemical potential. We set $\hbar = v_F = 1$.

however TF screening was not considered. We emphasize here that, because the TF contribution is of the same order of magnitude as the oscillatory part, it is essential to consider both of them. Furthermore we note that, while the TF contribution to screening given in Eq. (17) is independent of the dielectric constant ϵ_0 , the amplitude of the oscillatory part given in Eq. (18) decreases with increasing ϵ_0 . In fact, our numerical calculations show that for large distances the induced density does not change sign even in the hypothetical case of $\epsilon_0 = 0$ where the ratio between oscillatory and TF contribution would be maximal. This remarkable general property can be clearly appreciated in Fig. 3 for the particular case of $\epsilon_0 = 2.4$: The induced density $\delta n(r)$ does not change sign, but oscillates around a finite offset.

The polarization also determines the RKKY interaction energy between two magnetic impurities as well as the induced spin density due to a magnetic impurity, both quantities being proportional to the Fourier transform of $P^{(1)}(q, 0)$.¹⁷ For a magnetic impurity at \mathbf{r} the induced spin density $\delta m(\mathbf{r})$ is

$$\delta m(\mathbf{r}) \propto P^{(1)}(\mathbf{r}) = \frac{1}{4\pi^2} \int d^2 q P^{(1)}(q, 0) e^{i\mathbf{q} \cdot \mathbf{r}}. \quad (19)$$

Because we deal with $P^{(1)}$ instead of P_{RPA} , the TF contribution is missing. This results in an induced spin density that does oscillate around zero. Figure 4 shows the numerically calculated $P^{(1)}(r)$ and illustrates this behavior. Specifically in the long wavelength limit we obtain

$$\delta m(r) \propto \frac{\cos(2\mu r)}{r^3}, \quad (20)$$

which is clearly seen in the inset of Fig 4. Like for the induced charge density, we find that the induced spin polarization $\delta m(r)$ decreases like r^{-3} for large distances. Again, this contrasts with the r^{-2} behavior found in a

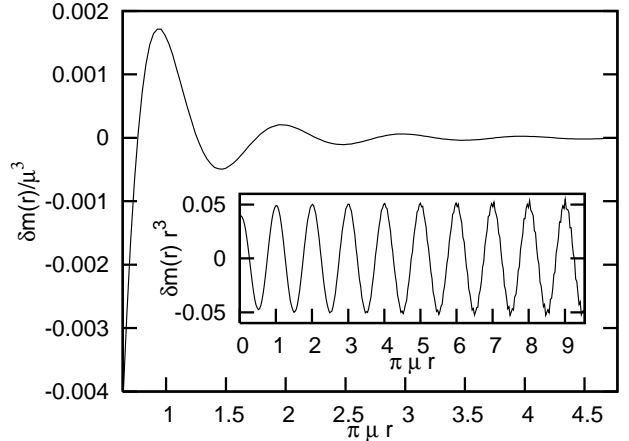


FIG. 4: Same as Fig. 3, for the induced spin density $\delta m(r)$.

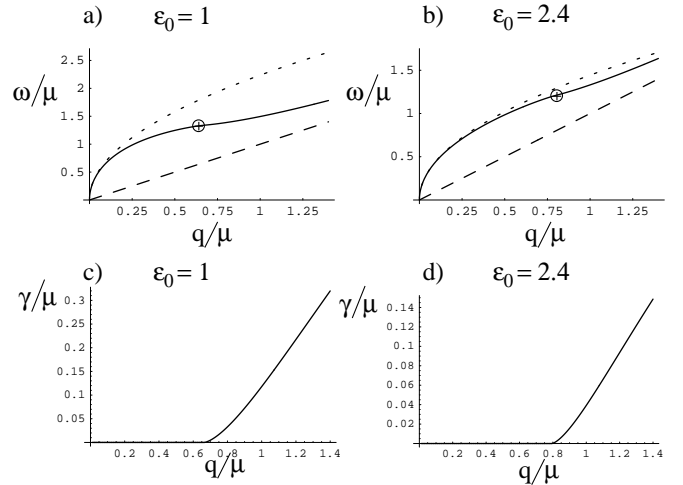


FIG. 5: Upper row: Solid lines show the dispersion relation for plasmons defined by $\text{Re } \epsilon(q, \omega) = 0$. Dotted lines show the low-q expansion of Eq. (22), while the dashed lines represents $\omega = v_F q$. The crosses indicate where the plasmons acquire a finite lifetime. Lower row: Decay rate γ of plasmons [see Eq. (21)] in units of chemical potential. We set $\hbar = v_F = 1$.

2DEG.¹⁷ For the particular case of undoped graphene we recover the monotonous r^{-3} decay obtained in Ref. 18.

Finally we note, that in contrast to the behavior of charge screening, where the induced charge scales like $1/\mu$ at large distances, the envelop function of the spin density is independent of the chemical potential at large distances.

IV. PLASMONS

The plasmon dispersion is determined by solving for $\epsilon(q, \omega_p - i\gamma) = 0$, where γ is the decay rate of the plasmons. For weak damping, the plasmon dispersion $\omega_p(q)$

and the decay rate γ are determined by¹³

$$\begin{aligned}\epsilon_0 &= v_q \operatorname{Re} P^{(1)}(q, \omega_p), \\ \gamma &= \frac{\operatorname{Im} P^{(1)}(q, \omega_p)}{\frac{\partial}{\partial \omega} \operatorname{Re} P^{(1)}(q, \omega) \big|_{\omega_p}}.\end{aligned}\quad (21)$$

Solutions to the first equation only exist for $\operatorname{Re} P^{(1)} > 0$, which is the case only for finite doping and $\omega > q$. Furthermore, a stable solution requires $\operatorname{Im} P^{(1)} = 0$, as is the case for region 1B of Fig. 6. Using the low- q expansion of the polarization given in Eq. (12), and neglecting the logarithmic correction, we obtain

$$\hbar\omega_p(q) = \left(\frac{g\alpha\hbar v_F q}{2\epsilon_0} \right)^{1/2}, \quad (22)$$

with α defined below Eq. (17). The \sqrt{q} behavior of the plasmon dispersion also appears in the 2DEG.

Outside region 1B, the plasmon is damped, i.e. it has a nonzero decay rate γ . This can be clearly seen in Figs. 2 and 5. In the upper row of Fig. 5, we plot the exact plasmon dispersion for two different values of ϵ_0 and indicate the point at which the collective excitation becomes damped. The lower row shows the decay rate as obtained from Eq. (21).

Finally, it is interesting to note that the combination of the linear dispersion relation for quasiparticles [electrons above (or holes below) the Fermi energy] and the plasmon dispersion makes it impossible for a quasiparticle of energy $\hbar\omega$ to decay into a plasmon with $q \leq \omega/v_F$. Hence, plasmons with infinite lifetime do not contribute to the lifetime of quasiparticles.

V. ACOUSTIC PHONONS AND SOUND VELOCITY

We now calculate the dispersion and the decay rate of acoustical phonons in graphene. We treat the electrons in the π -band of graphene as quasi-free electrons, while all the other electrons are assumed to be tightly bound to the carbon nuclei, thus forming effective ions with a positive elementary charge. In the absence of screening by the conduction electrons, the ions oscillate at their plasma frequency due to the long range nature of the Coulomb interaction. The collective modes of the combined electron-ion plasma can be obtained from the zeros of the total dielectric function $\epsilon_{\text{tot}}(q, \omega)$, which is obtained by summing the contributions from ions and electrons:¹⁹

$$\begin{aligned}\epsilon_{\text{tot}}(q, \omega) &= \epsilon_{\text{el}}(q, \omega) + \epsilon_{\text{ion}}(q, \omega) - 1 \\ &= \epsilon_0 - v_q [P_{\text{el}}(q, \omega) + P_{\text{ion}}(q, \omega)]\end{aligned}\quad (23)$$

Here P_{el} , ϵ_{el} are the polarization and the dynamical dielectric function of the electrons as given in Eqs. (9) and (16), while P_{ion} , ϵ_{ion} are the corresponding quantities for the ions. In the calculation of $P_{\text{ion}}(q, \omega)$ we

assume that the ions have a quadratic energy dispersion $E = \hbar^2 k^2 / 2M$ where M denotes the ion mass. The ionic charge density is two positive charges per unit cell, so that the Fermi wave vector of the ions is $k'_F \simeq (8\pi/A_c)^{1/2}$, where $A_c = 3\sqrt{3}a^2/2$ denotes the area of the hexagonal unit cell in real space.¹¹ This value of k'_F is exact for field effect doping and approximate for chemical doping.

In the calculation of P_{ion} we assume that, for all relevant frequencies, we can take $\omega \gg \hbar k'_F q / M$. In the case of acoustic phonons this assumption is equivalent to $v_s \gg \hbar k'_F / M \simeq 1.3 \times 10^{-4} v_F$, where v_s denotes the sound velocity. This relation is fulfilled for all meaningful dopings as shown below. In this regime the ion polarization is real and given by

$$P_{\text{ion}}(q, \omega) = \frac{k'_F^2 q^2}{4\pi M \omega^2} = \frac{2E_0 q^2}{\hbar^2 \omega^2}, \quad (24)$$

where we defined $E_0 = \hbar^2 / M A_c \simeq 7 \times 10^{-5}$ eV. We note that E_0 is of the order of the ion confinement energy.

We may estimate the dispersion and the decay rate of the acoustical phonons by inserting Eq. (23) into Eq. (21). For finite doping $\mu > 0$, the acoustic phonons at long wavelengths lie in the region 1A of Fig. 6 (defined by $\omega < v_F q < 2\mu/\hbar - \omega$), where $\operatorname{Re} P^{(1)}(q, \omega) = -g\mu/2\pi\hbar^2 v_F^2$. In this regime the phonon dispersion is easily obtained:

$$\omega_{\text{ph}} = \left(\frac{4\pi\alpha E_0}{\epsilon_0 \hbar v_F q + g\alpha\mu} \right)^{1/2} v_F q. \quad (25)$$

To be consistent with the precondition $\omega < v_F q$ the expression in the square root has to be smaller than one. This sets a lower limit to the values of the chemical potential for which Eq. (25) is valid. The sound velocity v_s and the decay rate γ may be derived from Eqs. (21) and (25) in the limit of low q . We obtain

$$v_s = \sqrt{\xi} v_F, \quad \gamma = \frac{\xi v_F q}{2\sqrt{1-\xi}}, \quad (26)$$

with $\xi = 4\pi E_0 / g\mu$.

Some additional remarks on the validity of Eq. (25) go in place. We have already said that, for $q \rightarrow 0$, it only applies provided $\xi < 1$. We also wish to note that the acoustical phonons are only well-defined if their frequency is much larger than their decay rate, i.e. if $\omega_{\text{ph}}/\gamma \gg 1$. Since $\omega_{\text{ph}}/\gamma = 1$ for $\xi = 4/5$, we conclude that the notion of acoustic phonons is justified for $\xi \ll 1$, which corresponds to $\mu \gg 4\pi E_0 / g \simeq 2.2 \times 10^{-4}$ eV. A detailed discussion of acoustical phonons for $\xi > 1$ is left for future work.

We have assumed initially that $v_s \gg \hbar k'_F / M \simeq 1.3 \times 10^{-4} v_F$. According to Eq. (26) this results in $\xi \gg 1.7 \times 10^{-8}$, or equivalently, $\mu \ll 10^8 E_0$, which is always fulfilled.

We finish this section by estimating the sound velocity of a typical graphene sample. Assuming a concentration

of "conduction-band" electrons of $n_{\text{el}} = 10^{10} - 10^{12} \text{ cm}^{-2}$ we get $\mu \simeq 10^{-2} - 10^{-1} \text{ eV}$. We note that this corresponds to $\xi \simeq 2 - 20 \times 10^{-3}$, so that Eqs. (25) and (26) are applicable, resulting in $v_s \simeq 0.05 - 0.14 v_F \simeq 4 - 12 \times 10^4 \text{ m/s}$ and $\gamma = 10^{-3} - 10^{-2} v_F q$. These results suggest a significant enhancement of the sound velocity, as compared to normal metals, where $v_s \simeq \sqrt{m/2M} v_F \lesssim 10^{-2} v_F$. The low polarizability of the conduction electrons leads to a poor screening of the oscillations of the charged ions. On the other hand, in a semiconductor with a gap larger than the typical acoustic phonon frequencies, the electrons follow adiabatically the ions. In that case, the lattice vibrations can be described as oscillations of neutral particles.

VI. CONCLUSIONS

In this article we have derived a compact and closed expression for the dynamical polarization of graphene within the RPA approximation. The obtained result is valid for arbitrary wave vector, frequency, and doping. As particular cases, we have derived the long-wavelength limit $q \rightarrow 0$ and the static limit $\omega \rightarrow 0$. We have employed the RPA polarization to calculate several physical quantities of interest in doped graphene. First we have studied the static Friedel oscillations of the induced charge(spin) density in the presence of a charged(magnetic) impurity. We have found that, although the charge density does show oscillations around an average value, it does it without changing sign. The reason for this remarkable behavior is that Friedel oscillations superpose on the dominant Thomas-Fermi induced density, with both contributions decaying at long distances r with the same power law r^{-3} .

The dynamical polarization has been used to calculate the dispersion relation and the decay rate of plasmons and acoustic phonons. Like in the 2DEG case, the plasmon frequency shows a \sqrt{q} -behavior in the long wavelength regime. We have determined the region in the (q, ω) plane where the plasmon is stable, as well as the decay rate in the regime where it is not.

The dispersion of acoustical phonons has been shown to be strongly dependent on the chemical potential. In particular, we have found that the sound velocity approaches the Fermi velocity at low doping. However, the same limit shows an increase in the decay rate of acoustic phonons due to electron-hole pair excitation.

Although we have focused on applications of the RPA calculation to the case of doped graphene, some aspects of the low-frequency, long-wavelength dynamics of pure graphene appear to be intriguing and worth studying further.

Note added. When this work was about to be submitted, we became aware of a related paper.²¹ Overlapping results in the two papers are in agreement.

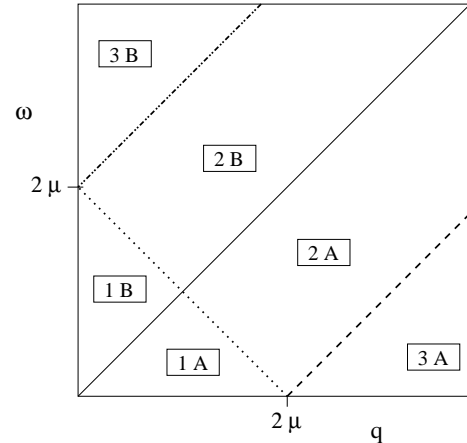


FIG. 6: Display of the different regions characterizing the susceptibility behavior. Regions are limited by straight lines $\omega = q$ (solid), $\omega = q - 2\mu$ (dashed) and $\omega = 2\mu - q$ (dotted). We set $v_F = \hbar = 1$.

Acknowledgements

We appreciate helpful discussions with A. H. Castro Neto. This work has been supported by the EU Marie Curie RTN Programme No. MRTN-CT-2003-504574, the EU Contract 12881 (NEST), and by MEC (Spain) through Grants No. MAT2002-0495-C02-01, FIS2004-06490-C03-00, FIS2005-05478-C02-01, and the Juan de la Cierva Programme.

APPENDIX A: CALCULATION OF THE POLARIZATION

In the following we present some major steps of the calculation of the polarization. We restrict the discussion to $\omega > 0$ since $P^{(1)}(q, -\omega) = [P^{(1)}(q, \omega)]^*$. In all the Appendix we set $v_F = \hbar = 1$.

1. Imaginary part

The imaginary part of the functions $\chi_D^\pm(q, \omega)$ defined in Eq. (5) has the following form

$$\text{Im}\chi_D^\beta(q, \omega) = -\frac{g}{4\pi} \int_0^D dk \sum_{\alpha=\pm} \alpha I^{\alpha\beta}(k, q, \omega),$$

$$I^{\alpha\beta} = k \int_0^{2\pi} d\varphi f^\beta(\mathbf{k}, \mathbf{q}) \delta[\omega + \alpha(k - \beta|\mathbf{k} + \mathbf{q}|)],$$

The φ -integration yields

$$I^{\alpha\beta} = \left[\frac{(2\alpha k + \omega)^2 - q^2}{q^2 - \omega^2} \right]^{\frac{1}{2}} \left\{ \Theta(\beta) \Theta(q - \omega) \Theta\left(k - \frac{q - \alpha\omega}{2}\right) \right. \\ \left. + \Theta(-\beta) \Theta(\omega - q) \Theta(-\alpha) \left[\Theta\left(\frac{\omega + q}{2} - k\right) - \Theta\left(\frac{\omega - q}{2} - k\right) \right] \right\},$$

which is always real. The final k -integration can now simply be performed. We obtain for $\mu = 0$

$$\begin{aligned} \text{Im}P_0^{(1)}(q, \omega) &= \frac{g}{4\pi} \int_0^\Lambda dk \sum_\alpha \alpha I^{\alpha-}(k, q, \omega) \\ &= -\frac{gq^2}{16\sqrt{\omega^2 - q^2}} \Theta(\omega - q). \end{aligned} \quad (\text{A1})$$

In order to present the result for $\mu > 0$, we introduce the real functions $f(q, \omega), G_>(x), G_<(x)$

$$\begin{aligned} f(q, \omega) &= \frac{g}{16\pi} \frac{q^2}{\sqrt{|\omega^2 - q^2|}}, \\ G_>(x) &= x\sqrt{x^2 - 1} - \cosh^{-1}(x), \quad x > 1, \\ G_<(x) &= x\sqrt{1 - x^2} - \cos^{-1}(x), \quad |x| < 1. \end{aligned} \quad (\text{A2})$$

For the additional term at finite doping given by Eq. (7), we obtain in the language of Fig. 6

$$\begin{aligned} \text{Im}\Delta P^{(1)}(q, \omega) &= -\frac{g}{4\pi} \int_0^\mu dk \sum_{\alpha, \beta} \alpha I^{\alpha\beta}(k, q, \omega) \\ &= f(q, \omega) \begin{cases} G_>(\frac{2\mu-\omega}{q}) - G_>(\frac{2\mu+\omega}{q}) & , 1 \text{ A} \\ \pi & , 1 \text{ B} \\ -G_>(\frac{2\mu+\omega}{q}) & , 2 \text{ A} \\ -G_<(\frac{\omega-2\mu}{q}) & , 2 \text{ B} \\ 0 & , 3 \text{ A} \\ 0 & , 3 \text{ B} \end{cases} \end{aligned}$$

2. Real part

The Kramers-Kronig relation valid for the retarded function $\text{Re}P_0^{(1)}(q, \omega)$ reads

$$\begin{aligned} \text{Re}P_0^{(1)}(q, \omega) &= \frac{1}{\pi} \int_{-\infty}^{\infty} d\omega' \frac{\text{Im}P_0^{(1)}(q, \omega')}{\omega' - \omega} \\ &= -\frac{gq^2}{16\sqrt{q^2 - \omega^2}} \Theta(q - \omega). \end{aligned} \quad (\text{A3})$$

For finite doping we rewrite Eq. (7) as

$$\begin{aligned} \text{Re}\Delta P^{(1)}(q, \omega) &= \frac{g}{4\pi^2} \int_0^\mu dk k \int_0^{2\pi} d\varphi \\ &\times \sum_{\alpha=\pm} \frac{2k + \alpha\omega + q \cos\varphi}{(k + \alpha\omega)^2 - |\mathbf{k} + \mathbf{q}|^2} . \end{aligned}$$

This integral is calculated directly such that the Kramers-Kronig relation is not needed, here. The φ -integration yields

$$\text{Re}\Delta P^{(1)} = -\frac{g\mu}{2\pi} + \frac{gsg_V}{8\pi^2} \sum_{\alpha=\pm} \int_0^\mu dk J^\alpha(k, q, \omega), \quad (\text{A4})$$

where $J^\alpha(k, q, \omega)$ is given by

$$\begin{aligned} J^\alpha &= 2\pi \left[\frac{(2\alpha k + \omega)^2 - q^2}{\omega^2 - q^2} \right]^{\frac{1}{2}} \left\{ \Theta(q - \omega) \Theta\left(\frac{q - \alpha\omega}{2} - k\right) \right. \\ &\left. + \Theta(\omega - q) \left[\Theta(\alpha) + \Theta(-\alpha) \left(\Theta\left(\frac{\omega - q}{2} - k\right) - \Theta(k - \frac{\omega + q}{2}) \right) \right] \right\}. \end{aligned}$$

We thus get in the language of Fig. 6

$$\begin{aligned} \text{Re}\Delta P^{(1)}(q, \omega) &= -\frac{g\mu}{2\pi} \\ &+ f(q, \omega) \begin{cases} \pi & , 1 \text{ A} \\ -G_>(\frac{2\mu-\omega}{q}) + G_>(\frac{2\mu+\omega}{q}) & , 1 \text{ B} \\ -G_<(\frac{\omega-2\mu}{q}) & , 2 \text{ A} \\ G_>(\frac{2\mu+\omega}{q}) & , 2 \text{ B} \\ -G_<(\frac{\omega-2\mu}{q}) + G_<(\frac{2\mu+\omega}{q}) & , 3 \text{ A} \\ G_>(\frac{2\mu+\omega}{q}) - G_>(\frac{\omega-2\mu}{q}) & , 3 \text{ B} \end{cases} \end{aligned}$$

3. Analytic representation

Concerning the analytic representation of the results given in Eq. (9), we note the following properties (see e.g. Ref 20)

$$\begin{aligned} \Theta(x - 1) \cosh^{-1}(x) &= \ln(x + \sqrt{x^2 - 1}), \\ \Theta(1 - x^2) \cos^{-1}(x) &= -i \ln(x + i\sqrt{1 - x^2}), \\ \cos^{-1}(-x) &= \pi - \cos^{-1}(x). \end{aligned}$$

Thus the functions $G_>(x), G_<(x)$ can be comprised by the single function $G(x) = x\sqrt{x^2 - 1} - \ln(x + \sqrt{x^2 - 1})$ where

$$G(x) = \begin{cases} G_>(x) & ; x > 1 \\ iG_<(x) = -i[\pi + G_<(-x)] & ; |x| < 1 \end{cases} . \quad (\text{A5})$$

We also note the relation $f(q, \omega) = |F(q, \omega)|$, where $f(q, \omega)$ is the real function defined in Eq. (A2) while $F(q, \omega)$ is the complex function introduced in Eq. (8).

¹ K. S. Novoselov, A. K. Geim, S. V. Morozov, D. Jiang, Y. Zhang, S. V. Dubonos, I. V. Grigorieva, and A. A. Firsov,

Science **306**, 666 (2004); K. S. Novoselov, A. K. Geim, S. V. Morozov, D. Jiang, M. I. Katsnelson, I. V. Grigorieva,

S. V. Dubonos, and A. A. Firsov, *Nature* **438**, 197 (2005); Y. Zhang, Y.-W. Tan, H. L. Stormer, and P. Kim, *Nature* **438**, 201 (2005).

² P. R. Wallace, *Phys. Rev.* **71**, 622 (1947).

³ J. W. McClure, *Phys. Rev.* **108**, 612 (1957).

⁴ J. González, F. Guinea, and V. A. M. Vozmediano, *Nucl. Phys. B* **424**, 595 (1994).

⁵ T. Ando, *J. Phys. Soc. Jap.* **75**, 074716 (2006).

⁶ K. W.-K. Shung, *Phys. Rev. B* **34**, 979 (1986); *ibid.* 1264 (1986); M. F. Lin and K. W.-K. Shung, *Phys. Rev. B* **46**, 12656 (1992).

⁷ D. P. DiVincenzo and E. J. Mele, *Phys. Rev. B* **29**, 1685 (1984).

⁸ M. I. Katsnelson, cond-mat/0609026.

⁹ K. Nomura and A. H. MacDonald, cond-mat/0606589

¹⁰ K. Nomura and A. H. MacDonald, *Phys. Rev. Lett.* **96**, 256602 (2006).

¹¹ N. M. R. Peres, F. Guinea, and A. H. Castro Neto, *Phys. Rev. B* **73**, 125411 (2006).

¹² G. D. Mahan, *Many-Particle Physics* (Plenum, New York, 1990).

¹³ A. L. Fetter, and J. D. Walecka, *Quantum Theory of Many-Particle Systems* (Dover, New York, 2003).

¹⁴ M.J. Lighthill, *Introduction to Fourier Analysis and Generalized Functions* (Cambridge University Press, Cambridge, 1958).

¹⁵ F. Stern, *Phys. Rev. Lett.* **18**, 546 (1967).

¹⁶ V. V. Cheianov and V. I. Fal'ko, cond-mat/0608228.

¹⁷ B. Fischer and M. W. Klein, *Phys. Rev. B* **11**, 2025 (1975); M. T. Béal-Monod, *Phys. Rev. B* **36**, 8835 (1987).

¹⁸ V. A. M. Vozmediano, M. P. López-Sancho, T. Stauber, and F. Guinea, *Phys. Rev. B* **72**, 155121 (2005).

¹⁹ N. W. Ashcroft and N. D. Mermin, *Solid State Physics* (Holt-Saunders, New York, 1976).

²⁰ M. Abramowitz and I. A. Stegun, *Handbook of Mathematical Functions* (Dover, New York, 1972).

²¹ E. H. Hwang and S. Das Sarma, cond-mat/0610561.